arXiv:1911.01107v1 [astro-ph.EP] 4 Nov 2019

Hot Oxygen and Carbon Escape from the Martian Atmosphere

H. Gröller[a], H. Lichtenegger[*a], H. Lammer[a], V. I. Shematovich[b]

[a] *Space Research Institute, Austrian Academy of Sciences, Schmiedlstrasse 6, A-8042 Graz, Austria*
[b] *Institute of Astronomy, Russian Academy of Sciences, 48 Pyatnitskaya St. 119017, Moscow, Russia*

Abstract

The escape of hot O and C atoms from the present martian atmosphere during low and high solar activity conditions has been studied with a Monte-Carlo model. The model includes the initial energy distribution of hot atoms, elastic, inelastic, and quenching collisions between the suprathermal atoms and the ambient cooler neutral atmosphere, and applies energy dependent total and differential cross sections for the determination of the collision probability and the scattering angles. The results yield a total loss rate of hot oxygen of $2.3 - 2.9 \times 10^{25}$ s^{-1} during low and high solar activity conditions and is mainly due to dissociative recombination of O_2^+ and CO_2^+. The total loss rates of carbon are found to be 0.8 and 3.2×10^{24} s^{-1} for low and high solar activity, respectively, with photodissociation of CO being the main source. Depending on solar activity, the obtained carbon loss rates are up to $\sim$ 40 times higher than the CO_2^+ ion loss rate inferred from Mars Express ASPERA-3 observations. Finally, collisional effects above the exobase reduce the escape rates by about 20-30% with respect to a collionless exophere.

Key words: Mars, hot atom escape, hot corona density, heavy atoms, oxygen, carbon

1. Introduction

The dynamics of the upper atmosphere and its interaction with the solar radiation and plasma environment are important clues for the stability and long-term evolution of terrestrial atmospheres. In a recent study Lammer et al. (2013) showed that the evolution and escape of the martian CO_2 atmosphere and the planet's H_2O inventory can be separated from the planet's origin into an early and a later evolutionary epoch. The first epoch started after Mars' formation and lasted $\leq$ 500 Myr (Lammer et al., 2013). Because of the high soft X-ray and EUV flux of the young Sun (e.g. Ribas et al., 2005; Claire et al., 2012) and Mars' low gravity the nebula-based and outgassed hydrogen-rich protoatmosphere was lost by hydrodynamic blow-off of H atoms and strong thermal escape rates of dragged heavier species such as O and C atoms within several

[*]Principal corresponding author
Email address: herbert.lichtenegger@oeaw.ac.at (H. Lichtenegger)

10^4 years (Erkaev et al., 2013, this issue). These recent results are in support of the hypotheses of Tian et al. (2009) that early Mars could not build up a dense CO_2 atmosphere during the early Noachian.

However, after the planet lost its protoatmosphere the atmospheric escape rates were most likely balanced with the volatiles (H_2O, CO_2, etc.) which have been outgassed by volcanic activity and delivered by impacts until the activity of the young Sun decreased, so that the atmospheric sources could dominate over the losses $\sim 4 - 4.2$ Gyr ago (Lammer et al., 2013). If a secondary outgassed CO_2 atmosphere of several 100 mbar was indeed present at the end of the Noachian, its evolution during the second epoch which lasted from the end of the Noachian until today should have been determined by a complex interplay of various nonthermal atmospheric escape processes, impacts, carbonate precipitation, and serpentinization during the Hesperian and Amazonian epochs which led to the present day surface pressure (Chassefière and Leblanc, 2011a,b).

Atmospheres may get eroded through the loss of light particles like H or He, when their thermal velocities exceed the escape velocity at the exobase. Heavier species like O or C, are stronger bound to the planet and can therefore either directly escape through nonthermal processes like dissociative recombination of molecular ions or may form extended coronae which in turn can be eroded by the solar wind. From Mars Express ASPERA-3 data Barabash et al. (2007) estimated the present escape of CO_2^+ molecular ions and yield low escape rates of $\sim 8 \times 10^{22}\,s^{-1}$. Based on this rate these authors estimated that the fraction of CO_2^+ molecular ions lost to space since the end of the Noachian when the martian dynamo stopped to work would represent an equivalent surface pressure of only about $\sim 0.2 - 4$ mbar.

Lammer et al. (2013) compared these ion escape rates with atmospheric sputtering and exothermic escape processes of heavy neutrals and suggested that the loss of photochemically produced suprathermal atoms such as O, C may be responsible for the main loss of the martian CO_2 atmosphere at present and most likely also during the planet's history until thermal escape took over.

The simulation of this nonthermal photochemically related escape of heavy atmospheric atoms at terrestrial planets is not only challenged by the physical and chemical complexity of the upper atmosphere but is additionally hindered by our sparse knowledge of many of the processes which govern the direct escape of atmospheric constituents. Although Mars has been visited by many spacecraft for more than 40 years, observational data of the hot particle corona at Mars are still rather limited (e.g. Leblanc et al., 2006; Lichtenegger et al., 2006); the only recent observation of the extended oxygen corona of Mars was made with the Alice far-ultraviolet imaging spectrograph during the Rosetta swing-by of Mars (Feldman et al., 2011). Therefore, numerical modeling of exosphere densities and of escape rates are still little constrained and suffer from the various assumptions made by different authors.

The aim of this work is to obtain a better understanding on the escape of hot carbon and oxygen atoms from present Mars. For this purpose we consider a number of possible sources of hot O and C atoms in the thermosphere, calculate the production rate profiles and the energy distribution functions at the exobase for low and high solar activity conditions and discuss the associated escape fluxes and exosphere density profiles. Because there are little observational hints of the rotational and vibrational

excitation distributions of the particles and because these effects have negligible influence on the escape rates (Gröller et al., 2010), we assume all particles in the rotational and vibrational ground states.

The simulations are based – if available – on the most recent data for both the atmospheric input and the collision cross sections. The model is limited by various circumstances: (a) the background atmosphere is represented by 1D ion and neutral density profiles (i.e. all variables depend only on radial distance) assumed to be valid for 60° solar zenith angle, (b) the hot particles are treated as test particles, i.e. their influence on the background gas is neglected, (c) due to the lack of data, some types of collisions are simulated by using approximate values of the parameters (see Tables 9 and 10).

2. Hot Atom Modeling

2.1. Monte Carlo model

The simulation of the hot particle corona is initiated by calculating for a specific reaction the corresponding velocity distribution of the products at discrete altitudes between 130 km and 450 km above the surface. These products are represented by a number of particles (typically $\sim 10^4$ per 2.5 km altitude step) and their 3-dimensional motion is followed through the thermosphere up to 450 km in the gravitational field of Mars. On their way the hot particles can interact with the background neutral atmosphere via elastic, inelastic and quenching collisions and will loose on average part of their initial energy. Background particles which acquire an energy exceeding the thermal velocity of the atmospheric species upon collisions are also treated as new hot particles. The collision probability and energy transfer is calculated by means of total and differential cross sections. At the exobase (for comparison with other models) and at 380 km altitude, the energy distribution function of the suprathermal particles is determined which in turn serves as input for the exosphere density calculations. A more detailed description of the Monte-Carlo model can be found in Gröller et al. (2010) and Gröller et al. (2012).

Although some 3D simulation results of the martian thermosphere have been published in the recent past (Valeille et al., 2010; Yagi et al., 2012), our background thermosphere model is assumed to be spherically symmetric for various reasons: (a) we do not focus on local variations such as solar zenith angle effects; (b) the primary aim of our paper is the study of a number of chemical reactions producing hot particles in view of their relevance for escape as well as the treatment of the various types of collisions on the basis of total and differential cross sections rather than on hard sphere or universal potential models, and this analysis can be done most easily in 1D; (c) to facilitate the comparison with older models which are to a large extend 1D models; (d) due to the lack of sufficient observations, realistic 3D thermosphere models of Mars are yet difficult to construct.

2.2. Input Profiles

The neutral and ion density as well as the temperatures for both high and low solar activity are taken from Fox and Hać (2009) for a solar zenith angle of 60 °. In their

model, the ambipolar diffusion for ions and the molecular and eddy diffusion for neutrals are included as well as more than 220 reactions. The altitude dependent density profiles of the background atmosphere are based on measurements of the Viking 1 neutral mass spectrometer together with simulations of the Mars Thermospheric General Circulation Model (MTGCM). According to Fox and Hać (2009), the O_2^+ density profiles measured by Viking can only be reproduced by imposing an upward velocity boundary condition ("eroded" ionospheres); therefore, only these eroded models are used in the present paper as input for the ion densities.

The solar flux is taken from the *Solar Irradiance Platform (SIP)* version 2.36 (Tobiska, 2004), where we have chosen DOY 32 of 2002 to represent high solar activity (HSA) and DOY 110 of 1997 to represent low solar activity (LSA). For these dates, HSA and LSA correspond to a solar flux of $F_{10.7} = 245.6$ and $F_{10.7} = 69.7$, respectively. Finally, for each considered neutral element in the atmosphere, the corresponding photo cross sections are taken from the *photo ionization/dissociation rates* database of Huebner et al. (1992).

2.3. Sources of Hot O Atoms

Although dissociative recombination (DR) of O_2^+ ions is supposed to be the main source of hot oxygen atoms (e.g. McElroy, 1972; Nagy and Cravens, 1988; Kim et al., 1998; Fox and Hać, 2009; Gröller et al., 2010, 2012), we have also considered some additional possible sources of hot O provided that the corresponding density profiles are available. These additional reactions are listed in Tables 2 to 6.

2.3.1. Dissociative and Radiative Recombination

Dissociative recombination of ground-state O_2^+ proceeds via the five exothermic channels shown in Table 1. The excited states $O(^1D)$ and $O(^1S)$ are 1.97 eV and

Table 1: Excess energies (e.g. Fox and Hać, 2009) and branching ratios (Peverall et al., 2001) for dissociative recombination of $O_2^+(X^2\Pi_g)$. The branching ratios correspond to approximately zero collision energy.

Reaction	**Channels**	**Excess Energy [eV]**	**Branching Ratios [%]**
$O_2^+ + e$	$O(^3P) + O(^3P)$	6.99	20.4
	$O(^3P) + O(^1D)$	5.02	44.0
	$O(^1D) + O(^1D)$	3.05	31.5
	$O(^3P) + O(^1S)$	2.80	0.0
	$O(^1D) + O(^1S)$	0.83	4.1

4.19 eV above the ground state $O(^3P)$, respectively. For the ground vibrational state of the oxygen molecule $O_2^+(v = 0)$, the branching ratios are taken from Peverall et al. (2001) for an electron-ion collision energy of nearly 0 eV. There are more recent values published by Petrignani et al. (2005) but they state that "The branching fractions and quantum yields do not entirely agree with earlier measurements from our group that were taken at energies between 0 and 40 meV in a cold ion beam, nor with measurements performed at ASTRID by Kella et al. (1997)." Therefore and because the listed branching ratios are comparable to those of Kella et al. (1997), the values from Peverall et al. (2001) are chosen.

The dissociative recombination of CO_2^+ and the corresponding excess energies and branching ratios are listed in Table 2. The branching ratios are taken from Viggiano et al. (2005), where the uncertainties are given in parentheses. Of all channels, only the third and fourth produce atomic oxygen, although the latter is of no interest since it is an endothermic process and its probability is close to zero.

The channels for dissociative recombination of NO^+ are given in Table 3. The branching ratios taken from Vejby-Christensen et al. (1998) are valid for the vibrational ground state and for an electron-ion collision energy close to 0 eV. The excited states $O(^1D)$ and $N(^2D)$ have energies of 1.97 eV and 2.38 eV above the corresponding ground states, respectively.

The excess energies and branching ratios for the dissociative recombination of CO^+ are listed in Table 4. The branching ratios for collision energies of 0.0, 0.4, 1.0, and 1.5 eV are taken from Rosén et al. (1998).

The altitude dependent production rate $P(r)$ of the dissociative recombination of an ion can be calculated by

$$P(r) = n_\mathrm{i}(r)\, n_\mathrm{e}(r)\, k(T_\mathrm{e}(r)), \tag{1}$$

where $n_\mathrm{i}(r)$ and $n_\mathrm{e}(r)$ are the altitude dependent ion and electron densities, respectively, and $k(T_\mathrm{e}(r))$ is the rate coefficient which depends on the electron temperature $T_\mathrm{e}(r)$. The value of k is determined according to the Arrhenius equation as

$$k(T_\mathrm{e}(r)) = \alpha \left(\frac{T_\mathrm{e}(r)}{300} \right)^\beta \qquad \mathrm{cm}^3\ \mathrm{s}^{-1}. \tag{2}$$

The coefficients α and β used for the dissociative recombination processes considered in this paper are listed in Table 5.

Another possible source of hot O is radiative recombination of O^+

$$O^+(^4S) + e \longrightarrow O(^3P) + h\nu,$$

where the parameters α and β for the rate coefficient (2) are taken from the UDFA06 database (Woodall et al., 2007) based on Nahar (1999) and given in Table 5. However, radiative recombination appears to be rather inefficient, yielding maximum production rates of about 1×10^{-4} and 2×10^{-5} $\mathrm{cm}^{-3}\ \mathrm{s}^{-1}$ for high and low solar activity, respectively.

The production rates as a function of altitude for the processes listed in Table 5 are illustrated in Figure 1 for low (a) and high (b) solar activity.

Table 2: Excess energies (e.g. Fox, 2004) and branching ratios (Viggiano et al., 2005) for dissociative recombination of CO_2^+; the uncertainties are given in parentheses.

Reaction	**Channels**	**Excess Energy [eV]**	**Branching Ratios [%]**
$CO_2^+ + e$	$CO_2(^1\Sigma_g)$	13.78	0.0 (+ 2.0)
	$C(^3P) + O_2(^3\Sigma_g)$	2.29	0.0 (+ 4.0)
	$CO(^1\Sigma) + O(^3P)$	8.27	100.0 (- 6.0)
	$C(^3P) + 2O(^3P)$	-2.87	0.0

Table 3: Excess energies and branching ratios (Vejby-Christensen et al., 1998) for dissociative recombination of $NO^+(X^1\Sigma^+)$; the latter are valid for zero electron-ion collision energy.

Reaction	Channels	Excess Energy [eV]	Branching Ratios [%]
$NO^+ + e$	$N(^4S) + O(^3P)$	2.78	15.0
	$N(^4S) + O(^1D)$	0.81	0.0
	$N(^2D) + O(^3P)$	0.39	85.0

2.3.2. Photodissociation

A further possible source of hot oxygen is photodissociation of O_2

$$O_2 + h\nu \longrightarrow O + O,$$

Table 4: Excess energies (e.g. Fox and Bakalian, 2001) and branching ratios (Rosén et al., 1998) for dissociative recombination of $CO^+(X^2\Sigma^+)$ for collision energies of 0.0, 0.4, 1.0, and 1.5 eV.

Reaction	Channels	Excess Energy [eV]	Branching Ratios [%]			
			0.0 eV	0.4 eV	1.0 eV	1.5 eV
$CO^+ + e$	$C(^3P) + O(^3P)$	2.90	76.1	53.0	39.0	38.0
	$C(^1D) + O(^3P)$	1.64	14.5	34.0	35.0	35.0
	$C(^3P) + O(^1D)$	0.93	9.4	8.0	15.0	11.0
	$C(^1S) + O(^3P)$	0.22	0.0	0.0	5.0	5.0
	$C(^1D) + O(^1D)$	-0.32		5.0	6.0	11.0
	$C(^3P) + O(^1S)$	-1.28				0.0

Table 5: Possible sources of hot O atoms due to dissociative and radiative recombination and references for the rate coefficients.

Source	Rate coefficient [$cm^3\,s^{-1}$]
Dissociative recombination	
$O_2^+ + e \longrightarrow O + O$	Sheehan and St.-Maurice (2004)
	$T \leq 1200\,K : \alpha = 2.40 \times 10^{-7}, \beta = -0.70$
	$T > 1200\,K : \alpha = 1.93 \times 10^{-7}, \beta = -0.61$
$CO_2^+ + e \longrightarrow CO + O$	Viggiano et al. (2005)
	$\alpha = 4.20 \times 10^{-7}, \beta = -0.75$
$NO^+ + e \longrightarrow N + O$	Sheehan and St.-Maurice (2004)
	$T \leq 1200\,K : \alpha = 3.50 \times 10^{-7}, \beta = -0.69$
	$T > 1200\,K : \alpha = 3.02 \times 10^{-7}, \beta = -0.56$
$CO^+ + e \longrightarrow C + O$	Rosén et al. (1998)
	$\alpha = 2.75 \times 10^{-7}, \beta = -0.55$
Radiative recombination	
$O^+ + e \longrightarrow O + h\nu$	Nahar (1999)
	$\alpha = 3.24 \times 10^{-12}, \beta = -0.66$

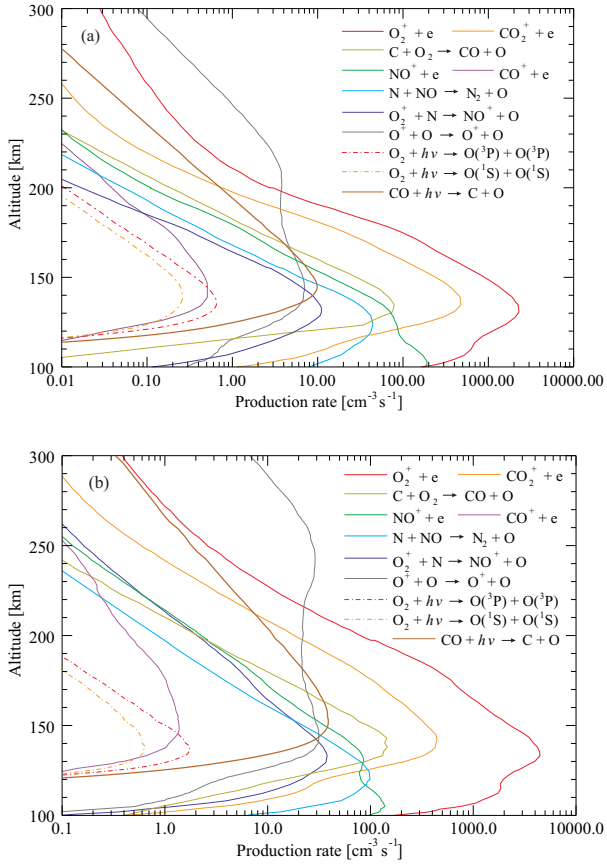


Figure 1: Production rates of hot O atoms for low (a) and high (b) solar activity due to various sources of oxygen.

for which an energy of at least 5.16 eV is needed (see *Bond Dissociation Energies in Simple Molecules* - B. deB. Darwent. NSRDS-NBS 31, (1970))[1].

The altitude dependent production rate $P(r)$ for photodissociation of a molecular neutral n can be obtained by the relation

$$P(r) = n_n(r) \int_\lambda \sigma_n^{\mathrm{pd}}(\lambda) F(r,\lambda)\, \mathrm{d}\lambda \tag{3}$$

where $n_n(r)$ is the altitude dependent neutral density, $F(r,\lambda)$ the solar flux at the altitude r and $\sigma_n^{\mathrm{pd}}(\lambda)$ the photodissociation cross section for the neutral at wavelength λ. The photodissociation and absorption cross sections are taken from Huebner et al. (1992)

[1] http://www.nist.gov/data/nsrds/NSRDS-NBS31.pdf

who provide them in the *Photo Rate Coefficient Database*[2].

For low and hight solar activity, the production rate of photodissociation of O_2 and CO valid for a solar zenith angle of 60° is illustrated in Figure 1. As can be seen, photodissociation of CO – though significant for the production of hot C (see Figure 2) – is of little importance for the production of hot O.

2.3.3. Chemical Reaction and Charge Transfer

The rate coefficient k for a two-body chemical reaction as well as for charge transfer is determined by means of the Arrhenius equation

$$k = \alpha \left(\frac{T}{300}\right)^{\beta} \exp\left(\frac{-\gamma}{T}\right) \qquad \mathrm{cm^3\ s^{-1}}, \tag{4}$$

where T is the gas temperature. The coefficients α, β, and γ are taken from the UDFA06 database described in Woodall et al. (2007) and are listed in Table 6. The production rate for the charge transfer between an ionized and a neutral oxygen atom is calculated using a rate coefficient equal to $1.6\times10^{-11}\,(T_\mathrm{n}+T_\mathrm{i})^{0.5}$ cm^3 s^{-1} taken from Terada et al. (2002) with T_n and T_i being the neutral and ion temperature, respectively.

Table 6: Possible sources of hot O atoms with their corresponding coefficients α, β, and γ to calculate the rate coefficient k in cm^3 s^{-1}. The excess energies for chemical reactions are given for the ground state of the products, e.g. O(^{3}P), CO($X^1\Sigma^+$).

Source	**Rate coefficient [cm^3 s^{-1}]**			**Production rate [cm^3 s^{-1}]**	
	α	β	γ	**HSA**	**LSA**
Chemical reaction					
$C + NO \longrightarrow CN + O + 1.22\,eV$	6.00×10^{-11}	−0.16	0.0	$<3\times10^{0}$	$<2\times10^{0}$
$C + O_2 \longrightarrow CO + O(^1D) + 4.04\,eV$	[a] 4.70×10^{-11}	−0.34	0.0	Figure 1b	Figure 1a
	[b] 2.48×10^{-12}	1.54	613.0	Figure 1b	Figure 1a
$C + O_2^+ \longrightarrow CO^+ + O + 4.04\,eV$	5.20×10^{-11}	0.00	0.0	$<5\times10^{-1}$	$<2\times10^{-1}$
$C^+ + O_2 \longrightarrow CO^+ + O + 3.23\,eV$	3.80×10^{-10}	0.00	0.0	$<2\times10^{0}$	$<10^{-1}$
$H + CO_2^+ \longrightarrow HCO^+ + O + 0.83\,eV$	2.90×10^{-10}	0.00	0.0	$<3\times10^{-1}$	$<2\times10^{0}$
$He^+ + CO \longrightarrow C^+ + O + He + 2.19\,eV$	1.60×10^{-9}	0.00	0.0	$<10^{-2}$	$<10^{-2}$
$He^+ + CO_2 \longrightarrow CO^+ + O + He + 1.04\,eV$	8.70×10^{-10}	0.00	0.0	$<10^{-2}$	$<10^{-2}$
$He^+ + NO \longrightarrow N^+ + O + He + 3.51\,eV$	1.40×10^{-9}	0.00	0.0	$<10^{-2}$	$<10^{-2}$
$He^+ + O_2 \longrightarrow O^+ + O + He + 5.81\,eV$	1.10×10^{-9}	0.00	0.0	$<10^{-2}$	$<10^{-2}$
$N + NO \longrightarrow N_2 + O + 3.26\,eV$	3.75×10^{-11}	0.00	26.0	Figure 1b	Figure 1a
$N + O_2^+ \longrightarrow NO^+ + O + 4.17\,eV$	1.80×10^{-10}	0.00	0.0	Figure 1b	Figure 1a
$N^+ + NO \longrightarrow N_2^+ + O + 2.23\,eV$	7.90×10^{-11}	0.00	0.0	$<10^{-4}$	$<3\times10^{-5}$
$N^+ + O_2 \longrightarrow NO^+ + O + 6.65\,eV$	2.63×10^{-10}	0.00	0.0	$<10^{-2}$	$<3\times10^{-3}$
Charge transfer					
$O^+ + H \longrightarrow H^+ + O + 0.02\,eV$	5.66×10^{-10}	0.36	−8.6	$<3\times10^{-2}$	$<2\times10^{-1}$
$O^+ + O_2 \longrightarrow O_2^+ + O + 1.55\,eV$	1.90×10^{-11}	0.00	0.0	$<10^{0}$	$<3\times10^{-2}$
$O^+ + O \longrightarrow O^+ + O + 0.00\,eV$	$1.6\times10^{-11}\,(T_\mathrm{n}+T_\mathrm{i})^{0.5}$			Figure 1b	Figure 1a

[a] for $T \le 300$K
[b] for $T > 300$K

[2] `http://phidrates.space.swri.edu (retrieved Nov 2012)`

Table 6 includes all oxygen producing reactions – besides photodissociation and the reactions listed in Tables 1-5 – which are considered in this study. We note that the second reaction in Table 6, i.e. $C(^3P) + O_2$ mainly produces excited $O(^1D)$ as measured by Ogryzlo et al. (1973) and Costes and Naulin (1998), although some portion of ground state $O(^3P)$ cannot be ruled out. For the present purpose we assume all oxygen products of this reaction beeing excited.

The change of enthalpy ΔH which is equal to the excess energy and listed in Table 6 is obtained via Hess's law. According to this law, the change of enthalpy for a chemical reaction can be calculated by means of the difference ΔH_f° between the heat of formation of the products and the heat of formation of the reactants, i.e.

$$\Delta H = \sum_{products} \Delta H_f^\circ - \sum_{reactants} \Delta H_f^\circ. \quad (5)$$

If ΔH is negative, the reaction is exothermic, otherwise it is endothermic. The values for the heat of formation ΔH_f° of the products and reactants are taken from the *CCCBDB (Computational Chemistry Comparison and Benchmark Database)* website[3].

Figure 1 also includes the production rates according to the reactions listed in Table 6 for which the maximum value is at least 1 $cm^{-3}\ s^{-1}$.

2.4. Main Sources of Hot C Atoms

2.4.1. Dissociative and Radiative Recombination

Dissociative recombination of CO_2^+ proceeds through the channels listed in Table 2. Atomic carbon is only produced via the second and fourth channel, however, since the fourth channel represents an endothermic process only the second channel is taken into account. The probability for this channel is low, however, because, as noted by Viggiano et al. (2005), it requires an unlikely rearrangement of the two oxygen atoms. The CO_2^+ ion is a linear molecule O=C=O^+ where the carbon is located in between the two oxygen atoms. In order to form the O_2 molecule, the two oxygen atoms have to bond in a very short time. It should be noted, however, that according to Seiersen et al. (2003) the branching ratio of the second channel is 9%, in contrast to almost zero percent as reported by Viggiano et al. (2005).

Dissociative recombination of CO^+ takes place via the channels shown in Table 4. C atoms can be produced in the ground state $C(^3P)$ and in the excited states $C(^1D)$ and $C(^1S)$. The latter states have energies of 1.26 eV and 2.68 eV, respectively, above the ground state.

Radiative recombination of C^+ proceeds via the reaction

$$C^+ + e \longrightarrow C(^3P) + h\nu,$$

where the parameters of equation (2) are taken from the UDFA06 database (Woodall et al., 2007) based on Nahar and Pradhan (1997). As for O^+, the production rates for radiative recombination of C^+ are low, having a maximum of $10^{-5}\ cm^{-3}\ s^{-1}$ at 150 km for high solar activity and of $3 \times 10^{-6}\ cm^{-3}\ s^{-1}$ at 140 km for low solar conditions.

[3]NIST Computational Chemistry Comparison and Benchmark Database. NIST Standard Reference Database Number 101 Release 15b, August 2011; Editor: Russell D. Johnson III; http://cccbdb.nist.gov/

The coefficients α and β for dissociative and radiative recombination are given in Table 7. The correponding atomic carbon production rates are illustrated in Figure 2 for low and high solar activity.

2.4.2. Photodissociation

In addition to dissociative recombination, photodissociation of CO is another important source of hot C atoms

$$CO + h\nu \longrightarrow C(^3P) + O(^3P)$$

with a threshold energy of 11.14 eV (see *Bond Dissociation Energies in Simple Molecules* - B. deB. Darwent. NSRDS-NBS 31, (1970))[4]. The production rate profiles of atomic carbon due to photodissociation of CO are included in Figure 2.

2.4.3. Chemical Reaction and Charge Transfer

The coefficients α, β, and γ for some additional reaction that produce hot atomic carbon are listed in Table 8. The corresponding production rates for high and low solar activity are also given, showing that hot carbon is created by these reactions with a low rate only; therefore they are not displayed in Figure 2.

2.5. Total and Differential Cross Sections

The motion of the hot particles through the thermosphere is dominated by collisions with the background atmosphere. Thus the appropriate treatment of collisions is a crucial task in the simulation of hot coronae. Depending on the collision model, e.g. a hard sphere approximation or energy dependent cross sections, a wide range of outcome can be obtained (e.g. Lichtenegger et al., 2009; Gröller et al., 2010). In the present paper, collisions are modeled by using total and differential cross sections.

Collisions between energetic particles and neutral background constituents can be either elastic, inelastic, or quenching. In elastic collisions the kinetic energy is conserved, only the scattering angle can change. During inelastic collisions kinetic energy

[4]http://www.nist.gov/data/nsrds/NSRDS-NBS31.pdf

Table 7: Possible sources of hot C atoms due to dissociative and radiative recombination and references of the rate coefficients.

Source	**Rate coefficient [cm^3 s^{-1}]**
Dissociative recombination	
$CO_2^+ + e \longrightarrow C + O_2$	Viggiano et al. (2005)
	$\alpha = 4.20 \times 10^{-7}, \beta = -0.75$
$CO^+ + e \longrightarrow C + O$	Rosén et al. (1998)
	$\alpha = 2.75 \times 10^{-7}, \beta = -0.55$
Radiative recombination	
$C^+ + e \longrightarrow C + h\nu$	Nahar and Pradhan (1997)
	$T \leq 7950\,\mathrm{K} : \alpha = 4.67 \times 10^{-12}, \beta = -0.60$

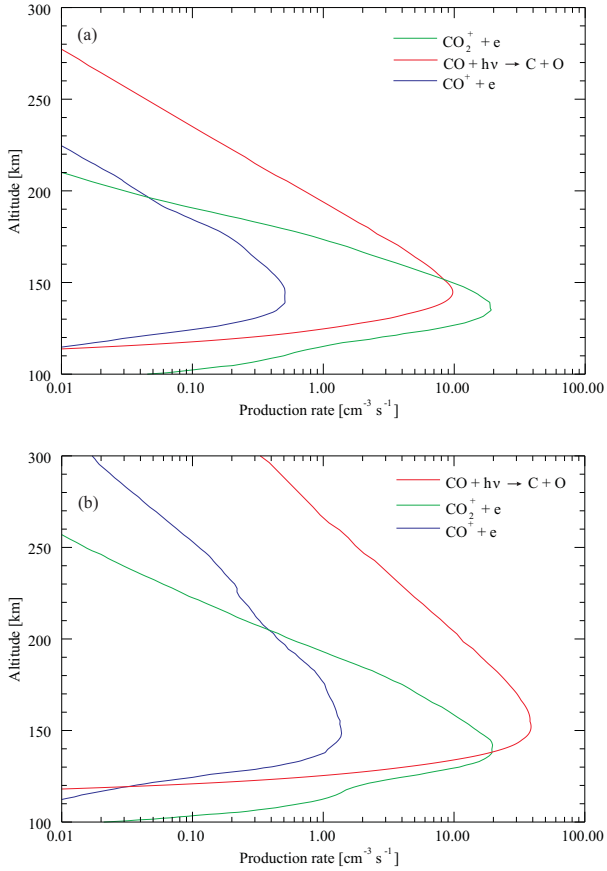


Figure 2: Production rates of hot C atoms for low (a) and high (b) solar activity due to different sources of carbon.

can be converted into vibrational energy and into electronic excitation, the latter being usually less likely. Quenching collisions describe the de-excitation of the reactant by collision, i.e. the conversion of the internal energy of the reactant into kinetic energy.

The references for the used total and differential collision cross sections (σ and dσ) as well as the fraction of energy (f_E) which goes into internal energy can be found in Tables 9 and 10. Inelastic collision of two oxygen atoms are not considered because the excitation energy in this case is higher than the energy released during the collision.

2.5.1. Collisions between O(^{3}P, ^{1}D, ^{1}S) and O

Collisions between energetic (hot) oxygen and a neutral thermal atom are either elastic

$$O_h(^3P,\ ^1D,\ ^1S) + A_{th} \rightarrow O_h(^3P,\ ^1D,\ ^1S) + A_h, \tag{6}$$

where A_{th} denotes the thermal background particles and O_h the hot oxygen, or quenching

$$O_h(^1D,\ ^1S) + A_{th} \rightarrow O_h(^3P) + A_h + \Delta E_q, \tag{7}$$

with the released energy ΔE_q being 1.97 eV and 4.19 eV for O(^{1}D) and O(^{1}S), respectively.

Since no data are available for the differential cross section of quenching collisions of excited O(^{1}D) and O(^{1}S) atoms, we assume them to be similar to the elastic collisions of O(^{1}D) atoms. The cross sections simulated by Yee and Dalgarno (1985), Yee and Dalgarno (1987), Yee et al. (1990), and Tully and Johnson (2001) for various types of collisions are illustrated in Figure 3a. Since hot particles may gain energies up to about 10 eV, the values for the cross sections are extrapolated to this interval.

2.5.2. Collisions between O(^{3}P, ^{1}D, ^{1}S) and N_2

Collisions between a suprathermal O atom and a neutral atmospheric background molecule can be

Table 8: Possible sources of hot C atoms and the corresponding coefficients α, β, and γ to calculate the rate coefficient k in cm^3 s^{-1}. The excess energies for chemical reactions are given for the ground state of the products, e.g. C(^{3}P), CO($X^1\Sigma^+$).

Source	**Rate coefficient [cm^3 s^{-1}]**			**Production rate [cm^3 s^{-1}]**	
	α	β	γ	**HSA**	**LSA**
Chemical reaction					
$C^+ + NO \longrightarrow NO^+ + C + 1.99\,eV$	5.20×10^{-10}	0.0	0.0	$< 6 \times 10^{-3}$	$< 4 \times 10^{-3}$
$He^+ + CO_2 \longrightarrow {O_2}^+ + C + He + 1.04\,eV$	1.10×10^{-11}	0.0	0.0	$< 10^{-4}$	$< 2 \times 10^{-4}$
$N^+ + CO \longrightarrow NO^+ + C + 0.67\,eV$	1.45×10^{-10}	0.0	0.0	$< 3 \times 10^{-2}$	$< 10^{-2}$

Table 9: Total and differential collision cross sections (σ, $d\sigma$) for elastic and quenching collisions between O atoms together with the available energy ranges.

Hot Particle	**Collision Type**	**References**
O(^{3}P)	elastic	Tully and Johnson (2001)
		σ: 1 – 10 eV *(Figure 4)*
		$d\sigma$: 1, 5, and 10 eV *(Figure 2)*
O(^{1}D)	elastic	Yee and Dalgarno (1987)
		σ: 0 – 5 eV *(Figure 4)*
		$d\sigma$: 0.1 and 1.0 eV *(Figure 2b and 3b)*
	quenching	Yee et al. (1990)
		σ: 0.001 – 5 eV *(Figure 4)*
		$d\sigma$: like O(^{1}D) elastic
O(^{1}S)	elastic	Yee and Dalgarno (1985)
		σ: 0 – 5 eV *(Figure 4)*
		$d\sigma$: 1 and 5 eV *(Figure 2b and 3b)*
	quenching	σ: like O(^{1}D) elastic
		$d\sigma$: like O(^{1}D) elastic

Table 10: Total and differential collision cross sections (σ, $d\sigma$) used in this study for elastic, inelastic, and quenching collisions between O and N_2, as well as the fraction (f_E) of the kinetic energy which changes into internal energy of the colliding molecule together with the available energy ranges.

Hot Particle	**Collision Type**	**References**
$O(^3P)$	elastic	Balakrishnan et al. (1998b)
		σ: 0 - 3 eV *(Figure 1)*
		Balakrishnan et al. (1998a)
		$d\sigma$: 1, 2, and 3 eV *(Figure 3 to 5)*
	inelastic	Balakrishnan et al. (1998b)
		σ: 0 - 3 eV
		$d\sigma$: 3 eV *(Figure 2)*
		f_E: 0 - 3 eV *(Figure 8)*
$O(^1D)$	elastic	Balakrishnan et al. (1999)
		σ: 0 - 2 eV *(Figure 1)*
		$d\sigma$: like $O(^3P)$
	inelastic	σ: like $O(^3P)$
		$d\sigma$: like $O(^3P)$
		Tachikawa et al. (1997)
		f_E: 0 - $\sim$ 0.8 eV *(Table 1)*
	quenching	Matsumi and Sarwaruddin Chowdhury (1996)
		σ: 0 - $\sim$ 0.9 eV *(Figure 9)*
		$d\sigma$: like $O(^3P)$
		Zahr et al. (1975)
		f_E: 0 - 1.2 eV *(Table II)*
$O(^1S)$	elastic, inelastic, and quenching	like $O(^1D)$

(a) elastic

$$O_h(^3P, ^1D, ^1S) + M_{th} \rightarrow O_h(^3P, ^1D, ^1S) + M_h, \tag{8}$$

where M_{th} denotes the thermal background molecule and O_h the hot oxygen atom,
(b) quenching

$$O_h(^1D, ^1S) + M_{th} \rightarrow O_h(^3P) + M_h + \Delta E_q, \tag{9}$$

with the released energy ΔE_q being a fraction of the excitation energies, or
(c) inelastic

$$O_h(^3P, ^1D, ^1S) + M_{th} \rightarrow O_h(^3P, ^1D, ^1S) + M_h - \Delta E_i, \tag{10}$$

where ΔE_i is the kinetic energy which is converted into internal energy of the products.

The total and differential collision cross sections for the collisions between $O(^3P, ^1D, ^1S)$ atoms and N_2 molecules are taken from the references listed in Table 10. In addition, energy ranges for which the cross sections are available are given together with the fraction f_E of the kinetic energy which goes into internal energy of the colliding molecule. The total collision cross section for inelastic $O(^3P)$–N_2 collisions is

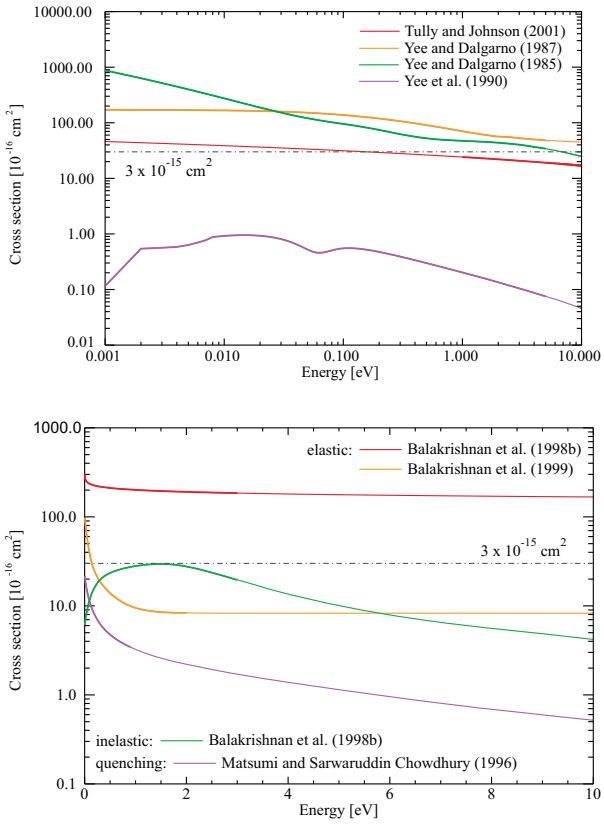


Figure 3: Total collision cross sections for (a) elastic and quenching collisions between O atoms, (b) elastic, inelastic, and quenching collisions between O atoms and N_2 molecules. The indicated constant value of 3×10^{-15} cm^2 was used by some others in the past.

calculated according to the fraction of the frequencies for elastic and inelastic collisions given in Figure 6 of Balakrishnan et al. (1998b). The fraction f_E of the energy which is deposited into N_2 vibrational and rotational excitation in percent of quenching $O(^1D)$–N_2 collisions is obtained from Figure 3 and Equation 4.2 of Zahr et al. (1975) for the three given collision energies of 0.03, 0.6, and 1.2 eV. For elastic collisions between $O(^3P)$ and N_2 no differential cross sections are available, therefore the differential cross sections for N–N_2 collisions published in Balakrishnan et al. (1998a) (Figures 3 to 5) are used. The cross sections of Zahr et al. (1975), Tachikawa et al. (1997), Balakrishnan et al. (1998b), and Balakrishnan et al. (1999) are based on simulations whereas those of Matsumi and Sarwaruddin Chowdhury (1996) are obtained from measurements. The total collision cross sections are shown in Figure 3b together with the constant cross section used by e.g. Fox and Hać (2009). Since the simulated particles can achieve energies up to about 10 eV, the cross sections are extrapolated to this interval.

2.5.3. Collisions between O(^{3}P, ^{1}D, ^{1}S) and other atoms and molecules

Due to the lack of data for collisions between hot oxygen and CO_2 or CO, the same total and differential cross sections and energy loss rates as for O−N_2 collisions are employed. Collisions of hot oxygen with H and He are treated by means of the elastic collision cross section for O−H collisions given in Zhang et al. (2009). For the collisions of hot oxygen atoms with other background atoms, the data for O−O collisions are used.

2.5.4. Collisions between C(^{3}P, ^{1}D, ^{1}S) and atoms or molecules

Since no data for collisions between hot atomic carbon and atoms or molecules of the background atmosphere are available, the same total and differential cross sections and energy loss rates as for collisions of hot oxygen with atoms and molecules are assumed, see Tables 9 and 10.

3. Results and Discussion

According to the input parameters used in our simulations, the calculated exobase altitude for low and high solar activity at Mars is located at about 220 and 260 km, respectively, above the surface. Once the energy distribution functions of hot O and C atoms at the exobase, at 380 km and at 450 km altitude are determined, escape fluxes as well as density profiles of the suprathermal atoms can be estimated. Assuming that the SZA=60° eroded models represent an average over the martian dayside, global escape rates are obtained by integrating the escape fluxes based on the according EDF and by multiplying the resulting total escape flux by the hemispheric area of Mars.

Table 11: Escape fluxes and hemispheric loss rates of hot oxygen atoms according to the present study. The numbers are based on the EDFs at the exobase altitude, 380 km and 450 km altitude, respectively.

Source	**Escape flux [cm^{-2} s^{-1}]**			**Escape rate [s^{-1}]**		
			Low solar activity			
	220 km	**380 km**	**450 km**	**220 km**	**380 km**	**450 km**
$O_2^+ + e \longrightarrow O + O$	1.8×10^7	1.4×10^7	1.3×10^7	1.5×10^{25}	1.2×10^{25}	1.2×10^{25}
$CO_2^+ + e \longrightarrow CO + O$	1.5×10^7	1.2×10^7	1.1×10^7	1.3×10^{25}	1.0×10^{25}	1.0×10^{25}
$O_2 + C \longrightarrow CO + O(^1D)$	8.4×10^5	6.1×10^5	5.8×10^5	6.9×10^{23}	5.5×10^{23}	5.3×10^{23}
$O_2^+ + N \longrightarrow NO + O$	1.0×10^5	0.7×10^5	0.7×10^5	0.8×10^{23}	0.6×10^{23}	0.6×10^{23}
total	$\mathbf{3.4 \times 10^7}$	$\mathbf{2.7 \times 10^7}$	$\mathbf{2.5 \times 10^7}$	$\mathbf{2.9 \times 10^{25}}$	$\mathbf{2.3 \times 10^{25}}$	$\mathbf{2.3 \times 10^{25}}$
			High solar activity			
	260 km	**380 km**	**450 km**	**260 km**	**380 km**	**450 km**
$O_2^+ + e \longrightarrow O + O$	2.5×10^7	2.1×10^7	2.0×10^7	2.1×10^{25}	1.9×10^{25}	1.9×10^{25}
$CO_2^+ + e \longrightarrow CO + O$	1.3×10^7	1.0×10^7	1.0×10^7	1.1×10^{25}	0.9×10^{25}	0.9×10^{25}
$O_2^+ + N \longrightarrow NO + O$	11.4×10^5	9.2×10^5	8.5×10^5	9.6×10^{23}	8.2×10^{23}	7.8×10^{23}
$O_2 + C \longrightarrow CO + O(^1D)$	8.1×10^5	5.9×10^5	5.5×10^5	6.8×10^{23}	5.2×10^{23}	5.1×10^{23}
total	$\mathbf{4.0 \times 10^7}$	$\mathbf{3.3 \times 10^7}$	$\mathbf{3.1 \times 10^7}$	$\mathbf{3.4 \times 10^{25}}$	$\mathbf{2.9 \times 10^{25}}$	$\mathbf{2.9 \times 10^{25}}$

Table 12: Comparison of hot oxygen escape rates of various studies due to DR of O_2^+ for low (LSA) and high solar activity (HSA).

References	**Escape rate $\times 10^{25}$ s^{-1}**	
	LSA	**HSA**
present study (at the exobase level)	1.5	2.1
present study (at 450 km)	1.2	1.9
Kim et al. (1998)[a]	3.4	8.5
Hodges (2000)[b]	2.8	-
Hodges Jr. (2002)[c]	4.4	18.0
Krestyanikova and Shematovich (2006)[d]	4.5	-
Cipriani et al. (2007)[e]	3.4	8.5
Cipriani et al. (2007)[f]	0.55	2.6
Chaufray et al. (2007)[g]	1.0	4.0
Fox and Hać (2009)[h]	0.66	0.68
Fox and Hać (2009)[i]	14.4	21.0
Valeille et al. (2010)[j]	3.8	13
Yagi et al. (2012)[k]	2.9 - 5.3	-

[a] corrected by a factor of 6.5 by Nagy et al. (2001); two-stream model and constant collision cross section of 1.2×10^{-15} cm^2

[b] constant collision cross section of 2×10^{-15} cm^2 for O−O and O−CO_2

[c] constant collision cross section of 2×10^{-15} cm^2 for O−O and O−CO_2 and including quenching of O(^{1}D) and O(^{1}S)

[d] Model B: including elastic, inelastic and quenching collisions; collision cross sections are taken from Balakrishnan et al. (1998b) and Kharchenko et al. (2000)

[e] atmosphere inputs from Kim et al. (1998) (corrected values) and the collision cross sections taken from Kharchenko et al. (2000) and Tully and Johnson (2001)

[f] atmosphere inputs from Krasnopolsky (2002) and the collision cross sections taken from Kharchenko et al. (2000) and Tully and Johnson (2001)

[g] single interaction potential and only atomic background atmosphere

[h] eroded ion profiles, exobase approximation, isotropic scattering and constant collision cross section of 3×10^{-15} cm^2

[i] eroded ion profiles, forward scattering using differential cross sections from Kharchenko et al. (2000) and constant collision cross section of 3×10^{-15} cm^2

[j] 3D thermospheric inputs from Bougher et al. (2006); constant collision cross section of 2×10^{-15} cm^2 for O−O and O−CO_2 collisions

[k] universal potential model for collisions; variations due to different martian seasons

3.1. Hot O Atoms

The escape fluxes together with the escape rates for various sources of hot oxygen are listed in Table 11 for LSA and HSA. Since the escape rates are calculated from the EDF, they depend on the altitude at which the EDF is taken. At sufficiently high altitudes, however, where collisions become insignificant, the escape rates converge towards a constant value. To illustrate this effect, the escape rates based on the EDFs at three different altitudes are shown in Table 11.

Although the production rates are generally larger during HSA, there is little difference in the escape of hot O between HSA and LSA. This is mainly due to the fact that at HSA also the neutral background density is higher, leading to an increase in the number of collisions between the suprathermal particles and the cold atmosphere and thus to a more efficient thermalization of the hot particles compared to LSA conditions. It should be noted that this effect is only found for the eroded ionosphere models. In case of the non-eroded ionosphere models of Fox and Hać (2009) the higher production rates of hot O at HSA is not totally compensated by the more efficient thermalization in the denser atmosphere; indeed in that case the escape rate of hot oxygen produced from O_2^+ is about 65% higher at HSA than at LSA.

Moreover, inspection of Table 11 also reveals that the escape flux due to DR of CO_2^+ is smaller for HSA than for LSA. This is due to the fact that the production rates in the region close to the exobase are comparable for LSA and HSA (∼0.1 and ∼0.3 $cm^{-3}\ s^{-1}$), while the initial energies of the newly produced hot O is different because of the different ion temperatures at LSA and HSA. The loss rates for both solar conditions are mainly sustained by particles with initial energies between $4.7 \lesssim E \lesssim 5.8$ eV whose production rates are higher at LSA than at HSA. Thus, although the number of particles with $E > 5.8$ eV is increased at HSA with respect to LSA, the number of particles with $E < 5.8$ eV is decreased, leading to a net escape flux at HSA smaller than at LSA.

The same effect can also be seen for the O_2 + C reaction. In case of O_2^+ + N, however, the escape flux for HSA is higher than for LSA. In this case, the effect of the initial energy distribution plays a minor role with respect to the higher production rate at higher altitudes.

Table 11 also illustrates the effect of ignoring the production of hot particles and their collisions with the background atmosphere above the exobase. The loss rates are found to be higher when based on the EDF at the exobase than when based on the EDF at 450 km altitude. This shows that the hot particles produced above the exobase only marginally contribute to the total escape despite the fact that most of these particles will be lost to space if their energy exceeds the escape energy. Rather, the decrease of escaping oxygen due to energy loss in collisions above the exobase somewhat exceeds the gain due to production, so that the escape rate is in fact reduced at 450 km by $\sim 20-30\%$ with respect to the values at the exobase altitude. In general our simulation results suggest that collision effects are still noticeable up to $\sim 5-10$ scale heights above the exobase.

In Table 12 our escape rates are compared to previous simulations. The differences in the results mainly reflect the differences in the input neutral and ion density profiles and the different treatment of collisions. Although we use the neutral density

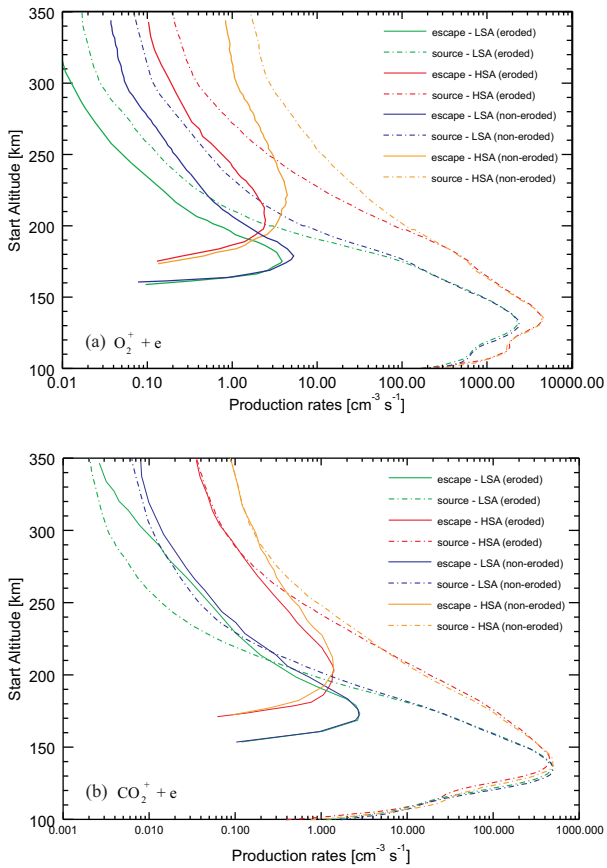


Figure 4: Production rates of escaping particles generated by DR of O_2^+ (a) and CO_2^+ (b) as a function of altitude for both solar activities and for the eroded and non-eroded ionosphere models. The dashed-dotted lines represent the production rates of all (escaping and non-escaping) oxygen atoms created via DR of O_2^+ (a) and CO_2^+ (b).

and ionosphere model of Fox and Hać (2009), the escape rates differ by a factor of 0.5 – 10. The main reason may be attributed to the different collision models: While Fox and Hać (2009) uses a constant collision cross section of 3×10^{-15} cm^2 for all types of collisions, we invoke different energy dependent collision cross sections (see Tables 9 and 10). In particular, the cross section for collisions with molecules – which are the most important types of collisions up to $\sim$ 200 km – is about one order of magnitude higher (see Figure 3b) than the above constant value. This higher value significantly increases the average number of collisions, thus leading to more efficient thermalization and to lower escape rates. Finally, while most previous studies reveal a distinct dependence of the hot oxygen loss rates on solar activity, this is neither the case in our results nor in those of Fox and Hać (2009) and may be attributed to the use of an eroded ionosphere model. Figure 4 illustrates the production rates of escaping O re-

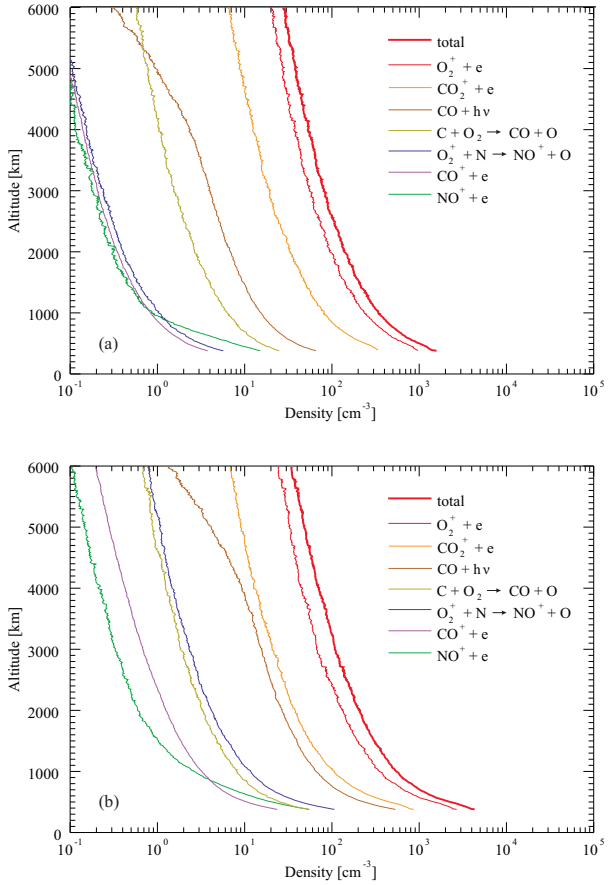


Figure 5: Exosphere densities of hot oxygen atoms for various sources for low (a) and high (b) solar activity.

sulting from the DR of O_2^+ and CO_2^+ as a function of altitude for both solar activities. For comparison, the results based on the eroded and non-eroded ionosphere models of Fox and Hać (2009) are shown. The solid lines represent the production rates at each height of those particles (consisting of hot particles generated by photochemical reactions and of background particles which became "hot" upon collisions with these particles) which arrive at 380 km altitude with an energy exceeding the escape energy. As can be seen, the production rates for the non-eroded models become larger than those for the eroded ones approximately at altitudes, where the O_2^+ density profiles become sensitive to the upward velocity. At higher altitudes, the production rate of escaping hot O created by collisions can even exceed the local production rate of O due to DR of CO_2^+.

The exosphere density profiles based on the energy distribution functions of hot oxygen at the exobase for low and high solar activity are shown in Figure 5. For both low and hight solar activity conditions the total exosphere density is mainly governed

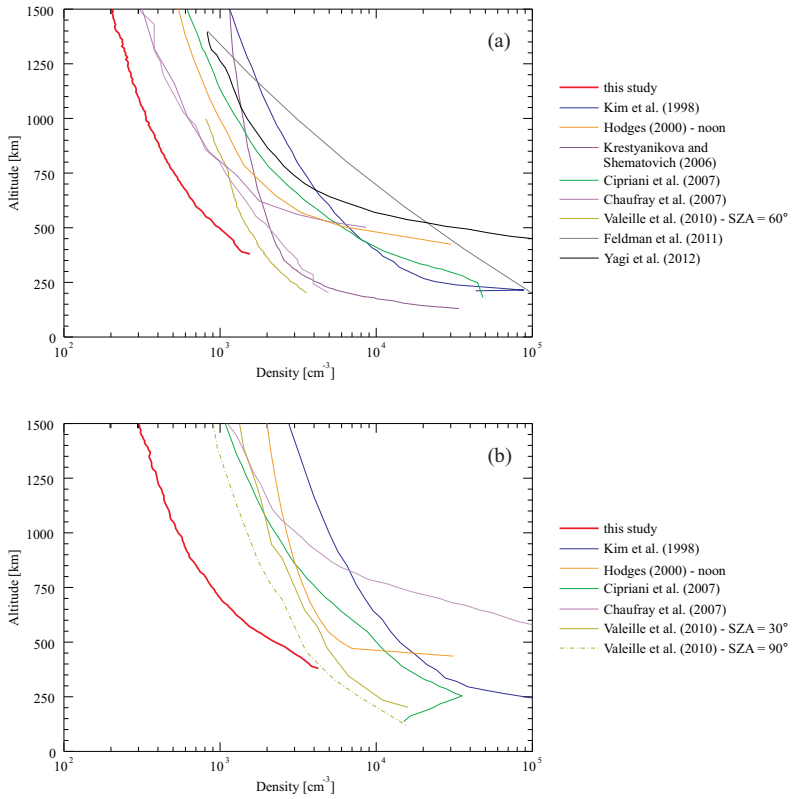


Figure 6: Comparison of exosphere densities of hot oxygen atoms for a number of studies. The curves of Hodges (2000), Chaufray et al. (2007), and Yagi et al. (2012) include also the cold component.

by DR of O_2^+ and CO_2^+. During HSA, however, at altitudes below $\sim$ 4000 km, the oxygen density due to photodissociation of CO becomes comparable with the density of O produced via DR of CO_2^+.

It should be noted that, although the production rate of hot O due to NO^+ + e is between one and two orders of magnitudes higher than the one due to CO^+ + e (see Figure 1), the obtained exosphere densities are comparable. The main reason is that the initial energies of the O atoms originating from NO^+ + e are on average much lower than those originating from CO^+ + e. Moreover, although the oxygen production rates due to the reactions C + O_2 and NO^+ + e are comparable above $\sim$ 130 km (Figure 1), the corresponding exosphere density arising from C + O_2 for HSA and LSA is nearly one order of magnitude higher than that arising from NO^+ + e (Figure 5).

This is due to the initial velocities of the oxygen atoms gained via DR of NO^+, which are much lower than those acquired via the reaction between C and O_2. Further, although the production rate of atomic oxygen originating from charge transfer between an ionized and a neutral O becomes dominant at higher altitudes (Figure 1), the contribution of this reaction to the exospheric density is negligible because the ini-

tial energies involved are similar to the average ion energies of ~ 0.3 eV. For HSA as well as LSA the production rate of oxygen atoms with an excess energy of 4.17 eV due to reaction $O_2^+ + N$ is about three orders of magnitude smaller than the production rate due to DR of of O_2^+ and thus leading also to much lower exosphere densities. Finally, at low solar activity, the oxygen exosphere density resulting from the reaction $O_2^+ + N$ is about 5-10 times smaller than the O density produced via $C + O_2$ (Figure 5a) because above ~ 130 km the production rate is also smaller by a similar amount (Figure 1a). At high solar activity, however, the production rates of these two reactions above ~ 180 km become comparable (Figure 1b), making also the densities comparable (Figure 5b).

In Figure 6 our exosphere densities are compared with previous studies. This Figure reflects the variety of results obtained based on different assumptions. The use of energy dependent total and differential cross sections and the inclusion of elastic, inelastic and quenching collisions as done in this study (see Tables 9 and 10) appear to favour lower exosphere densities than other assumptions (Table 12). In addition, in our simulations the collision of ground-state oxygen atoms with the atmospheric background is modeled by means of the total and differential cross sections of Tully and Johnson (2001) (see Table 9). As shown by Gröller et al. (2010) the use of the corresponding cross sections published by Kharchenko et al. (2000) would lead to somewhat higher densities.

3.2. Hot C Atoms

The escape fluxes as well as the escape rates for the most efficient sources of hot C are listed in Table 13. As opposed to oxygen, where DR of O_2^+ and CO_2^+ are the most important suppliers for hot O escape, the C loss is mainly due to photodissociation of CO. As in the case of oxygen, the higher production rates at HSA are at least partially compensated by the simultaneously increased number of collisions with the denser background atmosphere, leading to escape fluxes at HSA of about four times the flux at LSA. Regarding DR of CO_2^+, the corresponding carbon escape flux at HSA is even lower than at LSA. It should also be noted that the carbon production and escape rate due to photodissociation of CO, i.e. of a neutral molecule, is not affected by the erosion of the ionosphere, in contrast to the production and escape of oxygen due to DR of O_2^+- and CO_2^+-ions. Finally, the total loss rates calculated by means of the EDFs at 450 km altitude are about ~ 25 – 30% smaller than the loss rates obtained by using the EDFs at the exobase level. Thus collisions above the exobase are again still sufficient to reduce the flux of escaping carbon by a noticeable amount.

In Table 14 the escape rates of hot atomic carbon due to various source terms obtained in previous simulations are shown. As discussed in Fox (2004), a detailed analysis of the differences among the escape fluxes obtained by Nagy et al. (2001), Fox and Bakalian (2001), and Fox (2004) is difficult, but may be related to the use of different solar fluxes, dissociative recombination coefficients and exobase altitudes. The results of Cipriani et al. (2007) are significantly lower than the aforementioned values; unfortunately, these authors do not discuss any possible reasons for this discrepancy.

Upon comparing our computed carbon escape fluxes (Table 13) with those published in Fox (2004) (Table 14), it is seen that the fluxes at the exobase due to photodissociation of CO are higher by a factor of ~ 1.5 and ~ 1.3 for LSA and HSA,

Table 13: Escape fluxes and hemispheric loss rates of hot carbon atoms according to the present study. The numbers are based on the EDFs at the exobase altitude, 380 km and 450 km altitude, respectively.

Source	**Escape flux [cm^{-2} s^{-1}]**			**Escape rate [s^{-1}]**		
			Low solar activity			
	220 km	**380 km**	**450 km**	**220 km**	**380 km**	**450 km**
$CO + h\nu \longrightarrow C + O$	10.6×10^5	7.8×10^5	7.1×10^5	8.7×10^{23}	6.9×10^{23}	6.5×10^{23}
$CO_2^+ + e \longrightarrow O_2 + C^a$	1.4×10^5	1.0×10^5	0.9×10^5	1.1×10^{23}	0.9×10^{23}	0.8×10^{23}
$CO^+ + e \longrightarrow C + O$	0.8×10^5	0.7×10^5	0.6×10^5	0.7×10^{23}	0.6×10^{23}	0.6×10^{23}
total	$\mathbf{12.8 \times 10^5}$	$\mathbf{9.5 \times 10^5}$	$\mathbf{8.6 \times 10^5}$	$\mathbf{10.5 \times 10^{23}}$	$\mathbf{8.4 \times 10^{23}}$	$\mathbf{7.9 \times 10^{23}}$
			High solar activity			
	260 km	**380 km**	**450 km**	**260 km**	**380 km**	**450 km**
$CO + h\nu \longrightarrow C + O$	45.1×10^5	34.4×10^5	30.4×10^5	3.8×10^{24}	3.1×10^{24}	2.8×10^{24}
$CO^+ + e \longrightarrow C + O$	3.4×10^5	3.3×10^5	3.3×10^5	0.3×10^{24}	0.3×10^{24}	0.3×10^{24}
$CO_2^+ + e \longrightarrow O_2 + C^a$	1.2×10^5	0.8×10^5	0.8×10^5	0.1×10^{24}	0.1×10^{24}	0.1×10^{24}
total	$\mathbf{49.7 \times 10^5}$	$\mathbf{38.5 \times 10^5}$	$\mathbf{34.5 \times 10^5}$	$\mathbf{4.2 \times 10^{24}}$	$\mathbf{3.5 \times 10^{24}}$	$\mathbf{3.2 \times 10^{24}}$

[a]the branching ratio of this process is assumed to be 4%

respectively. Our escape fluxes at the exobase related to DR of CO_2^+ are about a factor of $\sim$ 4.5 and $\sim$ 2.4 higher for low and high solar activity, respectively, whereas our escape fluxes due to DR of CO^+ are about a factor of $\sim$ 1.6 and $\sim$ 2.3 lower than the one given in Fox (2004) who assumes the exobase locations at 184 and 220 km altitude for low and high solar acitivity. Besides the differences in the exobase heights, these latter lower values can be explained mainly by our lower production rates (Figure 1) which are based on the CO^+ density profiles of Fox and Hać (2009) being smaller than those given in Fox (2004).

The higher escape rates due to DR of CO_2^+ compared to Fox (2004) may be somewhat surprising at first glance, since we assume a branching ratio of only 4% for the C + O_2 channel of DR of CO_2^+, which is lower than the 9% assumed by Fox (2004). Moreover, our production rates of carbon are smaller than those calculated in Fox (2004) because we use the CO_2^+ profiles of Fox and Hać (2009) which correspond to lower densities than those in Fox (2004). That our escape rates of carbon produced by DR of CO_2^+ are nevertheless higher is at least partially due to the fact that we consider a higher initial velocity for carbon. While Fox (2004) assumes that the vibrational-rotational states of the resulting O_2 molecule and the translational states of the C and O_2 fragments are populated statistically, we assume O_2 to be in the electronic and vibrational-rotational ground state, which can be considered as an upper limit for the resulting velocities of the C atoms. In the latter case the velocity distribution peaks at $\sim$ 1.7 eV, in the former case at $\sim$ 0.6 eV. Another reason for our higher carbon escape rates is due to the different determination of these rates. Fox (2004) applies the exobase approximation, where the escape flux is estimated by integrating the production rates above the exobase. Our estimation, however, is based on the integration of the energy distribution function, yielding higher escape rates than the former method – especially in case of flat production rate profiles like the one for $CO_2^+ + e$.

Table 14: Escape fluxes of hot atomic carbon obtained in previous studies.

Reaction	**Escape flux $\times 10^5$cm^{-2} s^{-1}**	
	low solar activity	**high solar activity**
Nagy et al. (2001)[a]		
hemispheric escape fluxes		
$CO + h\nu \longrightarrow C + O$	-	60
$CO^+ + e \longrightarrow C + O$	-	17
total	**5.33**	**77**
Fox and Bakalian (2001)[b]		
global average escape fluxes[c]		
$CO + h\nu \longrightarrow C + O$	1.65	18
$CO^+ + e \longrightarrow C + O$	0.29	6.2
total	**1.94**	**24.2**
total (including additional sources)	**2.1**	**26**
Fox (2004)[b]		
hemispheric escape fluxes		
$CO + h\nu \longrightarrow C + O$	7.3	35
$CO^+ + e \longrightarrow C + O$	1.28	7.7
$CO_2{}^+ + e \longrightarrow C + O_2$	0.31	0.49
total	**8.89**	**43.19**
total (including additional sources)	**11.1**	**64**
Cipriani et al. (2007)[d]		
hemispheric escape fluxes[e]		
$CO^+ + e \longrightarrow C + O$	0.005	0.45

[a] cross section of 1.2×10^{-15} cm^2; for LSA only the sum of the rates for the two reactions is given by Nagy et al. (2001)

[b] cross section of 3×10^{-15} cm^2; exobase at $\sim$ 188 km for LSA and $\sim$ 220 km for HSA

[c] hemispheric escape fluxes are twice as large

[d] atmosphere inputs from Kim et al. (1998) and the collision cross sections used from Kharchenko et al. (2000) and Tully and Johnson (2001)

[e] calculated from the escape rates [s^{-1}] given in Table 1 of Cipriani et al. (2007) by dividing through the martian hemispheric surface at 400 km altitude

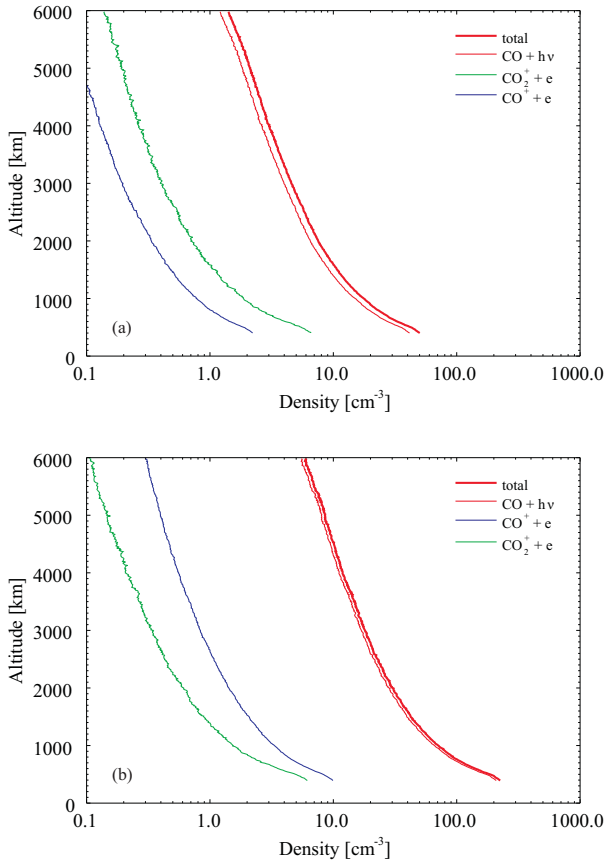


Figure 7: Exosphere densities of hot carbon atoms for various sources for low (a) and high (b) solar activity.

The exosphere density profiles for different source terms of the hot C atoms are shown in Figure 7 for low and high solar activity. In Figure 8 the carbon exosphere density obtained by a number of studies is illustrated. It should be noted that Nagy et al. (2001) include photodissociation of CO, dissociative recombination of CO^+ and collisions between energetic oxygen and thermal carbon atoms as sources of hot C, while Cipriani et al. (2007) consider only dissociative recombination of CO^+.

Our results suggest – in agreement with previous studies – that the main loss of atomic carbon at present Mars is due to photodissociation of CO. According to the present simulations, the total carbon loss is about 0.8 and $3.2 \times 10^{24}\,s^{-1}$ for low and high solar activity (Table 13) , respectively, which is $\sim 5-15$ times higher compared to the estimated average atmospheric sputtering of C atoms (Chassefière et al., 2007) and up to $\sim$ 40 times higher compared to the estimated CO_2^+ molecular ion escape from ASPERA-3 (Barabash et al., 2007). The present results are in accord with the suggestion of Lammer et al. (2013) that the escape of photochemically produced suprathermal

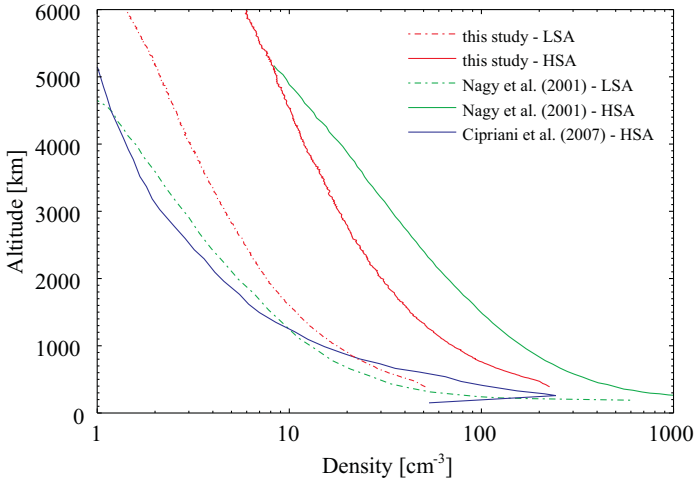


Figure 8: Comparison of the obtained exosphere densities of hot carbon atoms with previous studies.

C atoms, which originate from the dissociation of CO_2^+, CO^+ and CO are the most efficient processes for the loss of the martian CO_2 atmosphere at present. Therefore, these exothermic reactions may play a major role for the escape of the martian atmosphere since the end of the Noachian. It is important to note that the modeled hot C and O and the related CO_2 losses depend on a complex interplay of many physical and chemical processes – e.g. the change of the solar XUV flux and the corresponding response of the upper neutral and ionized atmosphere – and that the present escape rates can not be easily extrapolated backwards during the planet's history.

Since $CO_2^+ + e$ dissociates mainly into CO and O and only with 4% probability into C and O_2 (see Table 2), it follows O/C=24/1. On the other hand, the corresponding ratio of the escape rates (for e.g. LSA) is $1.0 \times 10^{25}/(0.8 \times 10^{23}) = 125$, i.e. oxygen can escape five times more efficient than carbon. This imbalance in the loss rates of O and C can be at least partially attributed to the difference in the energies released by the two channels producing atomic oxygen and carbon (Table 2), providing oxygen with a 3.3 times higher energy than carbon.

4. Summary and Conclusion

A number of possible sources for hot C and O atoms and the resulting escape rates during low and high solar activity conditions from present Mars have been studied by applying a Monte-Carlo model to simulate the stochastic motion of these particles through the upper atmosphere. The main sources of escaping oxygen are dissociative recombination of O_2^+ and CO_2^+ leading to a total loss of $\sim 2 - 3 \times 10^{25}\,s^{-1}$ over the solar cycle when an eroded ionosphere model is assumed. The vast majority of escaping carbon is delivered through photodissociation of CO with a total loss of the order of 0.5 to $3 \times 10^{24}\,s^{-1}$ over the solar cycle. This value is distinctly higher than the

estimated present loss due to atmospheric sputtering and the observed CO_2^+ escape at Mars.

The calculated loss rates based on the energy distribution function at 450 km altitude are reduced by $\sim 20 - 30\%$ with respect to the values calculated by means of the EDFs taken at the exobase level. This suggests that collisions still play a role above the exobase in a region with an extension of $\sim 5 - 10$ times the local scale height.

It should also be emphasized that the modeled oxygen loss is due to the reactions listed in Tables 1-6 – above all due to dissociative recombination of O_2^+ and CO_2^+ – and is therefore not directly related to the loss of water. On the other hand, the O escape cannot be balanced by C escape since the former appears to be 10–30 times higher than the latter. This suggests – assuming the martian atmosphere to be in steady state over long time scales – that all oxygen lost by escape may be finally replenished by means of H_2O via a hydrogen-carbon chemistry rather than converting CO_2 into CO, thereby stabilizing the CO_2 atmosphere.

Acknowledgement

The authors wish to thank two anonymous referees, whose constructive comments helped to improve the paper. H. Gröller, H. Lammer and H. Lichtenegger acknowledge support from the Helmholtz Alliance project "Planetary Evolution and Life", H. Gröller and H. Lichtenegger also acknowledge support by the Austrian Science Fund (FWF) under the project P24247-N16. H. Lammer acknowledges also the support by the FWF NFN project S116 "Pathways to Habitability: From Disks to Active Stars, Planets and Life", and the related FWF NFN subproject, S116607-N16 "Particle/Radiative Interactions with Upper Atmospheres of Planetary Bodies Under Extreme Stellar Conditions". V. Shematovich acknowledges support from the Basic Research Program of the Presidium of the Russian Academy of Sciences (Program 22), Russian Foundation for Basic Research (Project 11-02-00479a), Federal Targeted Program "Science and Science Education for Innovation in Russia 2009-2013".

References

Balakrishnan, N., Kharchenko, V., Dalgarno, A., 1998a. Quantum mechanical and semiclassical studies of $N+N_2$ collisions and their application to thermalization of fast N atoms. The Journal of Chemical Physics 108 (3), 943–949.

Balakrishnan, N., Kharchenko, V., Dalgarno, A., 1998b. Slowing of energetic $O(^3P)$ atoms in collisions with N_2. Journal of Geophysical Research 103 (A10), 23393–23398.

Balakrishnan, N., Kharchenko, V., Dalgarno, A., 1999. Translational energy relaxation of hot $O(^1D)$ atoms. The Journal of Physical Chemistry A 103, 3999–4001.

Barabash, S., Fedorov, A., Lundin, R., Sauvaud, J.-A., 2007. Martian atmospheric erosion rates. Science 315 (5811), 501–503.

Bauer, S. J., Lammer, H., 2004. Planetary Aeronomy - Atmosphere Environments in Planetary Systems. Springer.

Bougher, S. W., Bell, J. M., Murphy, J. R., Lopez-Valverde, M. A., Withers, P. G., 2004. Polar warming in the Mars thermosphere: Seasonal variations owing to changing insolation and dust distributions. Geophysical Research Letters 32, doi:10.1029/2005GL024059. L02203.

Chassefière, E., Leblanc, F., Langlais, B., 2007. The combined effects of escape and magnetic field histories at Mars. Planetary and Space Science 55 (3), 343–357.

Chassefière, E., Leblanc, F., 2011. Constraining methane release due to serpentinization by the observed D/H ratio on Mars. Earth and Planetary Science Letters 310, 262–271.

Chassefière, E., Leblanc, F., 2011. Explaining the redox imbalance between the H and O escape fluxes at Mars by the oxidation of methane. Planetary and Space Science 59, 218–226.

Chaufray, J. Y., Modolo, R., Leblanc, F., Chanteur, G., Johnson, R. E., Luhmann, J. G., 2007. Mars solar wind interaction: Formation of the Martian corona and atmospheric loss to space. Journal of Geophysical Research 112 (E9), E09009.

Cipriani, F., Leblanc, F., Berthelier, J. J., 2007. Martian corona: Nonthermal sources of hot heavy species. Journal of Geophysical Research 112 (E7), E07001.

Claire, M. W., Sheets, J., Cohen, M., Ribas, I., Meadows, V. S., Catling, D. C., 2012. The evolution of solar flux from 0.1 nm to 160 μm: Quantitative estimates for planetary studies. The Astrophysical Journal 757 (1), 95.

Costes, M., Naulin, C., 1998. State-to-state cross sections for the $C(^3P_J)$ + $O_2(X^3\Sigma_g^-) \longrightarrow CO(X^1\Sigma^+)$ + $O(^1D_2)$ reaction at kinetic energies between 4.4 and 90 meV. Comptes Rendus de l'Acadmie des Sciences - Series IIC - Chemistry 1 (12), 771–775.

Erkaev, N. V., Lammer, H., Elkins-Tanton, L., Odert, P., Kislyakova, K. G., Kulikov, Y. N., Leitzinger, M., Güdel, M., 2013. Escape of the martian protoatmosphere and initial water inventory. Planetary and Space Science, submitted.

Feldman, P. D. et al., 2011. Rosetta-Alice observations of exospheric hydrogen and oxygen. Icarus 214, 394–399.

Fox, J. L., 2004. CO_2^+ dissociative recombination: A source of thermal and nonthermal C on Mars. Journal of Geophysical Research 109 (A8), A08306.

Fox, J. L., Bakalian, F. M., 2001. Photochemical escape of atomic carbon from Mars. Journal of Geophysical Research 106 (A12), 28785–28795.

Fox, J. L., Hać, A. B., 2009. Photochemical escape of oxygen from Mars: A comparison of the exobase approximation to a Monte Carlo method. Icarus 204 (2), 527–544.

Gröller, H., Lammer, H., Lichtenegger, H. I. M., Pfleger, M., Dutuit, O., Shematovich, V. I., Kulikov, Y. N., Biernat, H. K., 2012. Hot oxygen atoms in the Venus nightside exosphere. Geophysical Research Letters 39 (3), L03202.

Gröller, H., Shematovich, V. I., Lichtenegger, H. I. M., Lammer, H., Pfleger, M., Kulikov, Y. N., Macher, W., Amerstorfer, U. V., Biernat, H. K., 2010. Venus' atomic hot oxygen environment. Journal of Geophysical Research 115, E12017.

Hodges, R. R., 2000. Distributions of hot oxygen for Venus and Mars. Journal of Geophysical Research 105 (E3), 6971–6981.

Hodges Jr., R. R., 2002. The rate of loss of water from Mars. Geophysical Research Letters 29 (3), 1038–1040.

Huebner, W. F., Keady, J. J., Lyon, S. P., 1992. Solar photo rates for planetary atmospheres and atmospheric pollutants. Astrophysics and Space Science 195 (1), 1–294.

Kella, D. P., Johnson, P. J., Pedersen, H. B., Vejby-Christensen, L., Andersen, L. H., 1997. The source of green light emission determined from a heavy-ion storage ring experiment. Science 276, 1530–1533.

Kharchenko, V., Dalgarno, A., Zygelman, B., Yee, J., 2000. Energy transfer in collisions of oxygen atoms in the terrestrial atmosphere. Journal of Geophysical Research 105 (A11), 24899–24906.

Kim, J., Nagy, A. F., Fox, J. L., Cravens, T. E., 1998. Solar cycle variability of hot oxygen atoms at Mars. Journal of Geophysical Research 103 (A12), 29339–29342.

Krasnopolsky, V. A., 2002. Mars' upper atmosphere and ionosphere at low, medium, and high solar activities: Implications for evolution of water. Journal of Geophysical Research 107 (E12), 5128.

Krestyanikova, M. A., Shematovich, V. I., 2006. Stochastic models of hot planetary and satellite coronas: A hot oxygen corona of Mars. Solar System Research 40 (5), 384–392.

Lammer, H., Chassefière, E., Karatekin, O., Morschhauser, A., Niles, P. B., Mousis, O., Odert, P., Möstl, U. V., Breuer, D., Dehant, V., Grott, M., Gröller, H., Hauber, E., Pham, L. B. S., 2013. Outgassing history and escape of the martian atmosphere and water inventory. Space Science Reviews 174 (1-4), 113–154.

Leblanc, F., Chaufray, J. Y., Lilensten, J., Witasse, O., Bertaux, J.-L., 2006. Martian dayglow as seen by the SPICAM UV spectrograph on Mars Expresss. Journal of Geophysical Research 111 (E9), E09S11.

Lichtenegger, H., Lammer, H., Kulikov, Y., Kazeminejad, S., Molina-Cuberos, G., Rodrigo, R., Kazeminejad, B., Kirchengast, G., 2006. Effects of low energetic neutral atoms on martian and venusian dayside exospheric temperature estimations. Space Science Reviews 126, 469–501.

Lichtenegger, H. I. M., Gröller, H., Lammer, H., Kulikov, Y. N., Shematovich, V. I., 2009. On the elusive hot oxygen corona of Venus. Geophysical Research Letters 36 (10), L10204.

Matsumi, Y., Sarwaruddin Chowdhury, A. M., 1996. Translational relaxation and electronic quenching of hot $O(^1D)$ by collisions with N_2. The Journal of Chemical Physics 104 (18), 7036–7044.

McElroy, M. B., 1972. Mars: An evolving atmosphere. Science 175 (4020), 443–445.

Nagy, A. F., Cravens, T. E., 1988. Hot oxygen atoms in the upper atmospheres of Venus and Mars. Geophysical Research Letters 15 (5), 433–435.

Nagy, A. F., Liemohn, M. W., Fox, J. L., Kim, J., 2001. Hot carbon densities in the exosphere of Mars. Journal of Geophysical Research 106 (A10), 21565–21568.

Nahar, S. N., 1999. Electron-Ion recombination rate coefficients, photoionization cross sections, and ionization fractions for astrophysically abundant elements. II. Oxygen ions. The Astrophysical Journal Supplement Series 120 (1), 131–145.

Nahar, S. N., Pradhan, A. K., 1997. Electron-Ion recombination rate coefficients, photoionization cross sections, and ionization fractions for astrophysically abundant elements. I. Carbon and nitrogen. The Astrophysical Journal Supplement Series 111 (1), 339–355.

Ogryzlo, E., Reilly, J., Thrush, B., 1973. Vibrational excitation of CO from the reaction $C + O_2$. Chemical Physics Letters 23 (1), 37–39.

Petrignani, A., Hellberg, F., Thomas, R. D., Larsson, M., Cosby, P. C., van der Zande, W. J., 2005. Electron energy-dependent product state distributions in the dissociative recombination of O_2^+. The Journal of Chemical Physics 122 (23), 234311–1–234311–8.

Peverall, R., Rosén, S., Peterson, J., Larsson, M., Al-Khalili, A., Vikor, L., Semaniak, J., Bobbenkamp, R., Le Padellec, A., Maurellis, A., van der Zande, W., 2001. Dissociative recombination and excitation of O_2^+: Cross sections, product yields and implications for studies of ionospheric airglows. The Journal of Chemical Physics 114 (15), 6679–6689.

Ribas, I., Guinan, E. F., Gudel, M., Audard, M., 2005. Evolution of the solar activity over time and effects on planetary atmospheres. I. High-energy irradiances (1-1700 Å). The Astrophysical Journal 622 (1), 680–694.

Rosén, S., Peverall, R., Larsson, M., Le Padellec, A., Semaniak, J., Larson, ., Strmholm, C., van der Zande, W. J., Danared, H., Dunn, G. H., 1998. Absolute cross sections and final-state distributions for dissociative recombination and excitation of CO^+(v=0) using an ion storage ring. Physical Review A 57 (6), 4462–4471.

Seiersen, K., Al-Khalili, A., Heber, O., Jensen, M. J., Nielsen, I. B., Pedersen, H. B., Safvan, C. P., Andersen, L. H., 2003. Dissociative recombination of the cation and dication of CO_2. Physical Review A 68 (2), 022708.

Sheehan, C. H., St.-Maurice, J., 2004. Dissociative recombination of N_2^+, O_2^+, and NO^+: Rate coefficients for ground state and vibrationally excited ions. Journal of Geophysical Research 109 (A3), A03302.

Tachikawa, H., Ohnishi, K., Hamabayashi, T., Yoshida, H., 1997. Translational relaxation of hot $O(^1D)$ by inelastic collision with N_2 molecule: Ab initio MO and classical trajectory studies. The Journal of Chemical Physics A 101, 2229–2232.

Terada, N., Machida, S., Shinagawa, H., 2002. Global hybrid simulation of the Kelvin−Helmholtz instability at the Venus ionopause. Journal of Geophysical Research 107 (A12), 1471.

Tian, F., Kasting, J. F., Solomon, S. C., 2009. Thermal escape of carbon from the early martian atmosphere. Geophysical Research Letters 36 (2), L02205.

Tobiska, W. K., 2004. SOLAR2000 irradiances for climate change research, aeronomy and space system engineering. Advances in Space Research 34 (8), 1736–1746.

Tully, C., Johnson, R. E., 2001. Low energy collisions between ground-state oxygen atoms. Planetary and Space Science 49 (6), 533–537.

Valeille, A., Combi, M. R., Tenishev, V., Bougher, S. W., Nagy, A. F., 2010. A study of suprathermal oxygen atoms in Mars upper thermosphere and exosphere over the range of limiting conditions. Icarus 206 (1), 18–27.

Vejby-Christensen, L., Kella, D., Pedersen, H. B., Andersen, L. H., 1998. Dissociative recombination of NO^+. Physical Review A 57 (5), 3627–3634.

Viggiano, A. A., Ehlerding, A., Hellberg, F., Thomas, R. D., Zhaunerchyk, V., Geppert, W. D., Montaigne, H., Larsson, M., Kaminska, M., Österdahl, F., 2005. Rate constants and branching ratios for the dissociative recombination of CO_2^+. The Journal of Chemical Physics 122 (22), 226101.

Woodall, J., Agúndez, M., Markwick-Kemper, A. J., Millar, T. J., 2007. The UMIST database for astrochemistry 2006. Astronomy and Astrophysics 466 (3), 1197–1204.

Yagi, M., Leblanc, F., Chaufray, J., Gonzalez-Galindo, F., Hess, S., Modolo, R., 2012. Mars exospheric thermal and non-thermal components: Seasonal and local variations. Icarus 221 (2), 682–693.

Yee, J., Dalgarno, A., 1985. Energy transfer of $O(^1S)$ atoms in collision with $O(^3P)$ atoms. Planetary and Space Science 33 (7), 825–830.

Yee, J., Guberman, S. L., Dalgarno, A., 1990. Collisional quenching of $O(^1D)$ by $O(^3P)$. Planetary and Space Science 38 (5), 647–652.

Yee, J. H., Dalgarno, A., 1987. Energy transfer of $O(^1D)$ atoms in collision with $O(^3P)$ atoms. Planetary and Space Science 35 (4), 399–404.

Zahr, G. E., Preston, R. K., Miller, W. H., 1975. Theoretical treatment of quenching in $O(^1D)$ + N_2 collisions. The Journal of Chemical Physics 62 (3), 1127–1135.

Zhang, P., Kharchenko, V., Jamieson, M. J., Dalgarno, A., 2009. Energy relaxation in collisions of hydrogen and deuterium with oxygen atoms. Journal of Geophysical Research 114 (A7), A07101.